catalysts

MDPI

Article

A Novel Tri-Coordination Zinc Complex Functionalized Silicotungstate with ROS Catalytic Ability and Anti-Tumor Cells Activity

Xiang Ma [1,2,†], Jiai Hua [1,*,†], Man Wang [3], Deqiang Zhang [1], Xinyao Pei [3], Xiaoyu Zhao [1], Yulan Niu [3,*] and Yanqing Wang [4,*]

[1] Department of Chemistry and Chemical Engineering, Taiyuan Institute of Technology, Taiyuan 030008, China; maxiang@tit.edu.cn (X.M.); zhangdeqiang0205@163.com (D.Z.); zhaoxiaoyu10140205@163.com (X.Z.)
[2] State Key Laboratory of Coordination Chemistry, Nanjing University, Nanjing 210023, China
[3] Laboratory of Biochemistry and Pharmacy, Taiyuan Institute of Technology, Taiyuan 030008, China; wangman3746@163.com (M.W.); peixinyao908@163.com (X.P.)
[4] School of Chemistry and Environmental Engineering, Yancheng Teachers University, Yancheng 224007, China
* Correspondence: huaja@tit.edu.cn (J.H.); niuyl@tit.edu.cn (Y.N.); wangyanqing@yctu.edu.cn (Y.W.); Tel.: +86-351-356-9476 (J.H.)
† These authors contributed equally to this manuscript.

Abstract: Reactive oxygen species (ROS) can be used as an effective method to treat tumors. Artificial oxidase has received increasing attention as a catalyst for ROS generation in fields ranging from bioinorganic chemistry to pharmaceutical chemistry. In this study, an artificial oxidase based on a binuclear zinc complex and Keggin-type silicotungstate $[Zn_2(4,4'\text{-bpy})(Phen)_2][SiW_{12}O_{40}]$ (ZSW) (4,4′-bpy = 4,4′-bipyridine; Phen = 1,10-phenanthroline) was synthesized and structurally featured in terms of its X-ray photoelectron spectrum (XPS), bond valence sum (Σ*s*) calculation, IR spectra, and single-crystal X-ray diffraction (SXRD). ZSW is an ionic compound in which the cation is a binuclear zinc complex $[Zn_2(4,4'\text{-bpy})(Phen)_2]^{4+}$ and the anion is a α-Keggin-type silicotungstate $[SiW_{12}O_{40}]^{4-}$ cluster. Notably, the Zn ions in the $[Zn_2(4,4'\text{-bpy})(Phen)_2]$ exist in tri-coordination, which was first obtained in polyoxometalate (POM) chemistry. It was also demonstrated that ZSW is capable of efficiently catalyzing the production of ROS, which, according to the computational calculations, may be due to the synergistic action of zinc complexes and POM building blocks. Furthermore, ZSW exhibited inhibition ability toward ROS-sensitive tumor cells, such as PC12 cells.

Keywords: silicotungstate; tri-coordination binuclear zinc; reactive oxygen species; artificial oxidase; anti-tumor ability

Citation: Ma, X.; Hua, J.; Wang, M.; Zhang, D.; Pei, X.; Zhao, X.; Niu, Y.; Wang, Y. A Novel Tri-Coordination Zinc Complex Functionalized Silicotungstate with ROS Catalytic Ability and Anti-Tumor Cells Activity. *Catalysts* **2022**, *12*, 695. https://doi.org/10.3390/catal12070695

Academic Editor: Annaluisa Mariconda

Received: 30 April 2022
Accepted: 17 June 2022
Published: 24 June 2022

1. Introduction

Reactive oxygen species (ROS), as the most common response medium in biochemistry, are ubiquitous in pathological procedures [1,2]. Hence, research on and developments of materials that are able to catalyze the production of ROS have attracted more and more attention from researchers and clinicians [3–5]. Metal ions, such as copper, iron, and manganese, are considered strong catalytic centers for the composition of reactive proteins in viable organisms that can produce ROS efficiently [6–8]. Recently, the synthesis of a series of ROS-catalyzing artificial enzymes has been achieved [9–11]. In such research, the study of copper complexes occupies a dominant position; however research on other essential bio-metal ions, such as zinc ions, is relatively behind [11]. Since zinc also exhibits excellent bio-activity [12], further research will likely lead to the construction of novel zinc complexes combined with catalysts capable of catalyzing ROS.

Polyoxometalates (POMs), a particularly attractive family of late metal oxygen clusters, possess multiform structures and various useful properties [13–16]. POMs have several features that allow them to act as bulky polydentate ligands; for example, nanosized

dimensions, an oxygen-abundant surface, nucleophilic properties, and poly-bond-making sites, which may allow them to bond with transition-metal ions in flexible coordination configurations [17–25]. Recent research has noted that the oxidation catalytic activity of Keggin-type POM fragments is remarkable [26,27] and that it could potentially facilitate the catalyzation of transition-metal ion-triggered production of ROS [28]. Moreover, these POMs can induce the formation of poly-nuclearity clusters of transition metal ions and, further, maintain these clusters for relatively long times [29]. Therefore, a hybrid molecule originating from Keggin-type POMs partnered with poly-nuclearity Zn clusters has the potential to retain the best characteristics of both base constituents, while also exhibiting additional positive characteristics.

In this work, a newly designed POM, $[Zn_2(4,4'\text{-bpy})(Phen)_2][SiW_{12}O_{40}]$ (ZSW) (Phen = 1,10-phenanthroline; 4,4′-bpy = 4,4′-bipyridine), was synthesized and studied. The new molecule was constructed from a pure inorganic structure Keggin-type silicotungstate anion $[SiW_{12}O_{40}]^{4-}$ and a binuclear zinc complex $[Zn_2(4,4'\text{-bpy})(Phen)_2]^{4+}$. Notably, ZSW is able to catalyze the production of ROS efficiently and exhibits activity that inhibits ROS-sensitive tumor cells, such as PC12 cells.

2. Results and Discussion

2.1. X-ray Single-Crystal Structures

In this study, SXRD was used to determine the structure of ZSW. The crystallographic data and selected bond lengths are given in Table 1 and Table S1, respectively. The data details were deposited at the Cambridge Crystallographic Data Centre with the CCDC number 2103951. As shown in Figure 1, X-ray structural analysis revealed that the unit of ZSW consists of two parts: the binuclear zinc complex $[Zn_2(4,4'\text{-bpy})(Phen)_2]^{4+}$ and the Keggin-type $[SiW_{12}O_{40}]^{4-}$ cluster.

Table 1. Crystallographic data and structural refinements for ZSW.

Empirical Formula	**$C_{68}H_{48}N_{12}O_{40}SiW_{12}Zn_4$**
Formula weight	4168.95
Crystal system	Orthorhombic
Space group	Ibam
a/Å	13.297(3)
b/Å	25.304(5)
c/Å	26.922(5)
α/deg	90
β/deg	90
γ/deg	90
V/Å^3	9058(3)
Z	4
D_c/g cm^{-3}	3.057
μ/mm^{-1}	16.308
T/K	296(2)
Limiting indices	$-15 \leq h \leq 15$ $-25 \leq k \leq 30$ $-32 \leq l \leq 28$
Measured reflections	22599
Independent reflections	4084
R_{int}	0.0403
Data/restraints/parameters	4084/12/326
GOF on F^2	1.051
Final R indices ($I > 2\sigma(I)$)	R_1 = 0.0310 wR_2 = 0.0956
R indices (all data)	R_1 = 0.0415 wR_2 = 0.1019

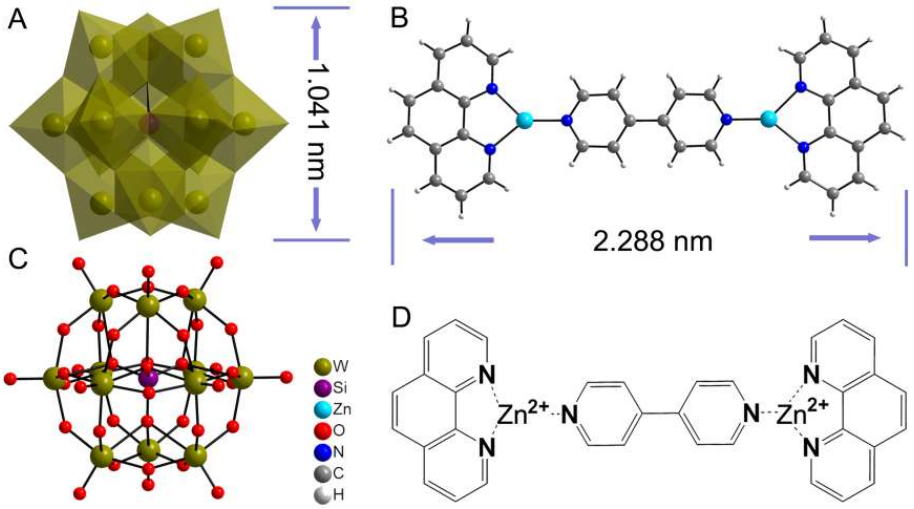

Figure 1. (**A**) Polyhedral view of the $[SiW_{12}O_{40}]^{4-}$ unit; (**B**) ball-and-stick view of the binuclear copper complex $[Zn_2(4,4'\text{-bpy})(Phen)_2]^{4+}$; (**C**) ball-and-stick view of the $[SiW_{12}O_{40}]^{4-}$ unit; (**D**) structural diagram of $[Zn_2(4,4'\text{-bpy})(Phen)_2]^{4+}$ in $[Zn_2(4,4'\text{-bpy})(Phen)_2][SiW_{12}O_{40}]$ (ZSW).

As shown in Figure 1B,D, the $[Zn_2(4,4'\text{-bpy})(Phen)_2]^{4+}$ in ZSW has an inversion center located at the center of the 4,4′-bpy ligand, which consists of two zinc ions, two Phen ligands and one 4,4′-bpy ligand. Each zinc ion is coordinated by three N atoms from the 4,4′-bpy and Phen ligands, with Cu–N distances ranging from 1.892 to 2.029 Å. The sum of the different angles around the Zn ion is 360°, which indicates a trigonal-planar geometry around the center metal ion. The roles of the Phen and 4,4′-bpy ligands coordinating with Zn^{2+} are different, with the 4,4′-bpy serving as a bridging ligand linking the two Zn^{2+} ions, while the two Phen ligands act as chelating agents coordinated with Zn^{2+}. Alternatively, the 4,4′-bpy ligand can join two $[Zn(Phen)]^{2+}$ ions to form a binuclear zinc complex.

In coordination chemistry, zinc ions always have a tetra-, penta-, and hexa-coordination configuration. The tri-coordination metal ion is usually the intermediate state in the REDOX process, such as Cu^{2+}-Cu^{+} [30]. To our knowledge, in the solid state, the stable tri-coordination zinc ion complex is very rare. Based on hybrid orbital theory, zinc ions in ZSW may adopt the sp^2 hybrid configuration, which has a p orbital perpendicular to the plane. The p orbital of C in the organic ligand is also perpendicular to the molecular plane. These p orbitals are parallel to each other and may form a conjugated π bond. Electrons on the π bond flow through the system, so it is possible that, at some point, the electron cloud on zinc will become a little denser, causing its valence state to deviate from +2, and this exchange of electrons through a conjugated π bond might improve the catalytic ability of zinc cores [31].

As shown in Figure 1A,C, tetrahedral $\{SiO_4\}$ is located at the center of the $[SiW_{12}O_{40}]^{4-}$ cluster and shares four oxygen atoms with four $\{Mo_3O_{13}\}$ triads. Those four $\{Mo_3O_{13}\}$ clusters are connected to each other by the sharing edge and O_μ, forming an α-Keggin-type cluster. The valence of the tungsten ions in ZSW was assessed using X-ray photoelectron spectroscopy (XPS). As shown in Figure 2, the XPS spectrum with two wide peaks located at 36.9 and 34.8 eV may have been caused by W $4f_{7/2}$ and W $4f_{5/2}$, respectively [32]. The fitted dashed plots in Figure 2 suggest the association of the W 4*f* peaks with W^{6+} [32]. These results imply that the +6 valence W ions are present in ZSW, as is evident from the peak intensities.

The bond valence sums (Σ*s*) of the oxygen (O) atoms in ZSW were also calculated using the method from [33]. Formula (1) is shown below:

$$V_i = \sum_j s_{ij} = \sum_j \exp\left(\frac{r_0' - r_{ij}}{B}\right) \quad (1)$$

in which r_{ij} is the detected and r_0' the theoretical bond distances between two atoms; B was set to 0.37 [34]. The theoretical values for $r_0'(W^{6+}–O)$ (1.906 Å), r_0' ($Si^{4+}–O$) (1.622 Å), and r_0' ($Zn^{2+}–N$) (1.770 Å) were obtained from the literature [34,35]. The calculations indicate that, for the W, Si, and Zn in ZSW, the Σs was 6.1678(4), 4.1078(8), and 1.7342(3), respectively.

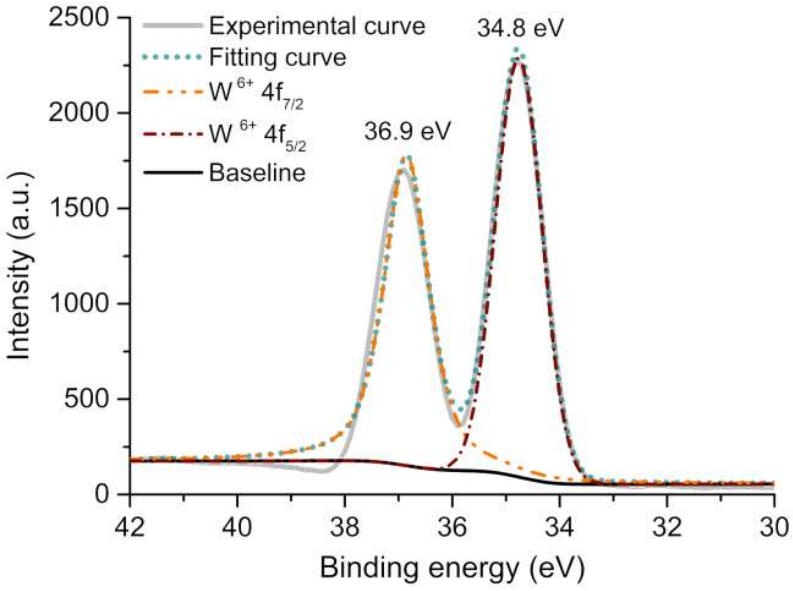

Figure 2. X-ray photoelectron spectrum (XPS) and the fitted curves of W in ZSW.

The computation of Σs can also be done using measured bond distances. The results are given in Table 2 and Figure 3. POMs can easily be protonated, as their fragments are highly negatively charged and contain abundant basic surface O atoms [36]. We can categorize the 40 O atoms in ZSW into terminal O_t and bridging $O_{\mu 2}$, $O_{\mu 3}$, and $O_{\mu 4}$ types. As shown in Figure 3, delocalized protons are located on the O atoms with Σs ranging between 0 and 1.70, which serve as proton-donors, while those O atoms with Σs ranging between 1.95 and 2.00 hold dense electrons. Multiple protons delocalized across the entire POM fragment is a frequent occurrence that has been described in many previous studies, such as $[Ni(enMe)_2]_3[H_6Ni_{20}P_4W_{34}(OH)_4O_{136}(enMe)_8(H_2O)_6]\cdot 12H_2O$ [33], $[H_3W_{12}O_{40}]^{5-}$ [37], and $[Ni(en)_3]_2[H_2Nb_6O_{19}]\cdot 8H_2O$ [38]. As these findings suggest, delocalization of a few counter-positive charges in ZSW occurs in the $[SiW_{12}O_{40}]^{4-}$ skeleton, which probably facilitates proton absorption and, by extension, valence state balancing upon valence alteration of metal ions [39].

Table 2. Bond valence and Σs of Si, W, Zn in ZSW.

Bond	Valence	Bond	Valence	Bond	Valence	Atom	Σs
Si (1)-O (4)	0.9246 (1)	Si (1)-O (8)	1.1293 (2)	Si (1)-O (4)#	0.9246 (1)		
Si (1)-O (8)#	1.1293 (2)					Si (1)	4.1078 (8)
W (1)-O (1)	1.8122 (9)	W (1)-O (2)	1.0027 (1)	W (1)-O (3)	1.0000 (0)		
W (1)-O (3)#	1.0000 (0)	W (1)-O (2)#	1.0027 (1)	W (1)-O (4)	0.2393 (7)		
W (2)-O (3)	1.0357 (5)	W (2)-O (8)	0.2165 (9)	W (2)-O (5)	1.7928 (1)	W (1)	6.0570 (1)
W (2)-O (6)	1.0844 (5)	W (2)-O (7)	1.0136 (1)	W (2)-O (12)#	1.0246 (2)	W (2)	6.2320 (1)
W (3)-O (7)	1.0218 (5)	W (3)-O (7)#	1.0218 (5)	W (3)-O (8)	0.2762 (3)	W (3)	6.1277 (7)
W (3)-O (8)#	0.2762 (3)	W (3)-O (10)	0.9602 (7)	W (3)-O (10)#	0.9602 (7)	W (4)	6.2426 (7)
W (4)-O (2)#	1.0218 (5)	W (4)-O (4)#	0.2868 (9)	W (4)-O (6)#	1.0218 (5)		
W (4)-O (10)	1.0583 (9)	W (4)-O (11)	1.8122 (9)	W (4)-O (12)	1.0413 (7)		
Zn (1)-N (1)	0.5185 (3)	Zn (1)-N (2)	0.7191 (1)	Zn (1)-N (3)	0.4965 (8)	Zn (1)	1.7342 (3)

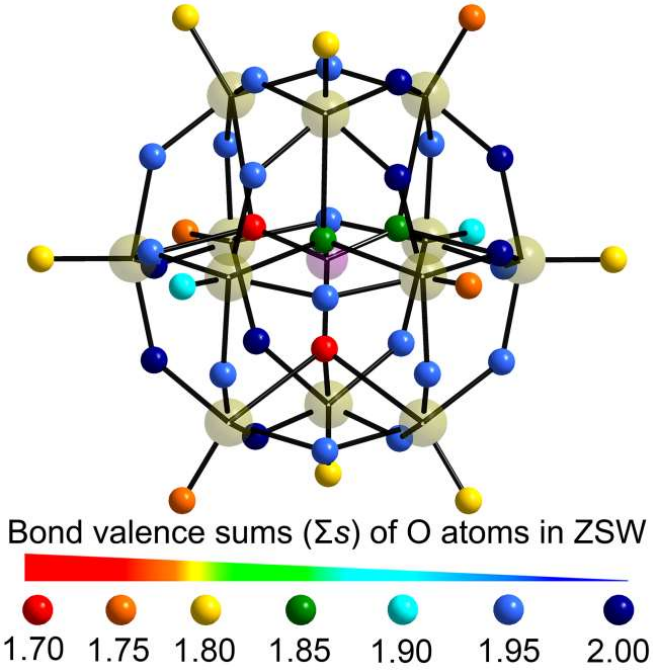

Figure 3. The bond valence sums (Σ*s*) of O atoms in the Keggin unit of [Zn_2(4,4′-bpy)$(Phen)_2$][$SiW_{12}O_{40}$] (ZSW). The extent of protonation for each oxygen atom is indicated by different colors.

The IR spectrum of ZSW has similar asymmetric vibrations to those silicotungstate-containing complexes [40]. As shown in Figure 4A, four characteristic peaks were observed at 1043, 938, 828, and ~722 cm^{-1}, which were assigned to v(Si–$O_{\mu4}$), v(W–O_t), v(W–$O_{\mu2}$), v(W–$O_{\mu3}$), and v(W–$O_{\mu4}$), respectively [40]. In comparison with those of the $[SiW_{12}O_{40}]^{4-}$ cluster, the ν(W–O_t) vibrational bands for ZSW are split, which may indicate structural distortion and a consequent reduction in symmetry [31]. The IR spectra of 4,4′-bpy and Phen were also tested and are shown in Figures S1 and S2. Comparing these IR spectra to ZSW, the peaks observed at 1616~1116 and 3300~3500 cm^{-1} in Figure 4A may be attributable to the peaks of 4,4′-bpy and Phen, which would be consistent with the literature [41]. PXRD was performed with the bulk samples. As shown in Figure 4B, the as-synthesized PXRD peaks of ZSW were basically consistent with the simulated ones.

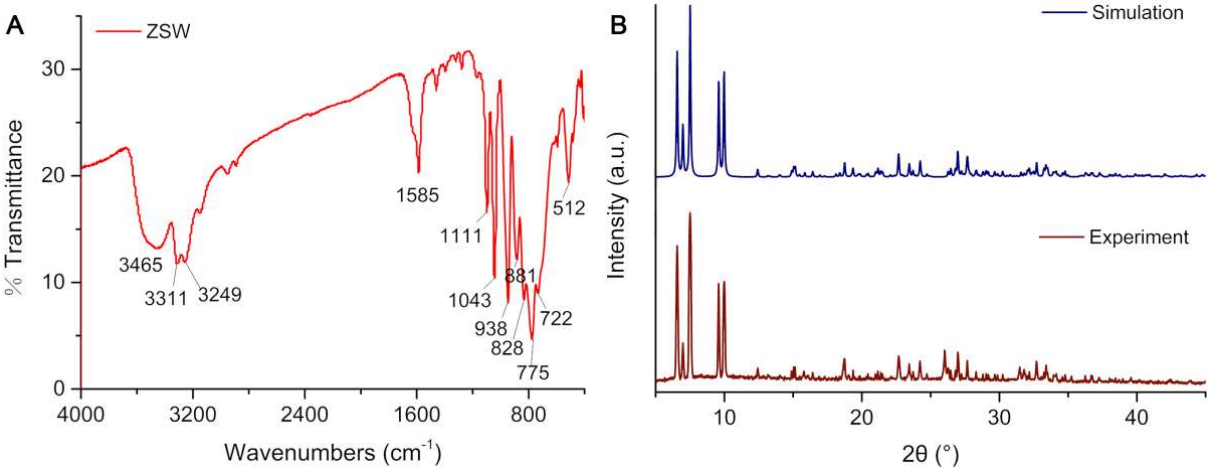

Figure 4. (**A**) IR spectrum for [Zn_2(4,4′-bpy)$(Phen)_2$][$SiW_{12}O_{40}$] (ZSW), 4,4′-bipyridine (4,4′-bpy), 1,10-phenanthroline (Phen); (**B**) PXRD patterns of ZSW.

2.2. Catalytic Property

A dichlorofluorescein (DCF) fluorescence assay was employed to study the ZSW-mediated production of ROS. DCF is a fluorescent probe derived from the reaction of DCFH-DA (non-fluorescent) with ROS in the presence of HRP, which can indicate the release of ROS from a system [42]. As seen in Figure 5, ZSW showed a stronger and more intense fluorescent spectrum (λ_{em} = 528 nm) than that of the control group, which suggests there was richer ROS production with ZSW than without. The $K_4[SiW_{12}O_{40}]$ (C1) and $ZnCl_2$ + Cyclen (ZnL) groups also possessed catalytic activity. However, the ZSW group showed three to four times more fluorescence than the C1 and ZnL groups. It is of note that the DCF fluorescence intensity of the Zn^{2+} group sample was extremely low, even lower than that of the control group, which indicated remarkably lower production of ROS by the group with Zn^{2+}. These phenomena can probably be attributed to the metal ion–HRP enzyme interaction, causing a loss in the Zn^{2+} group's catalytic properties [43].

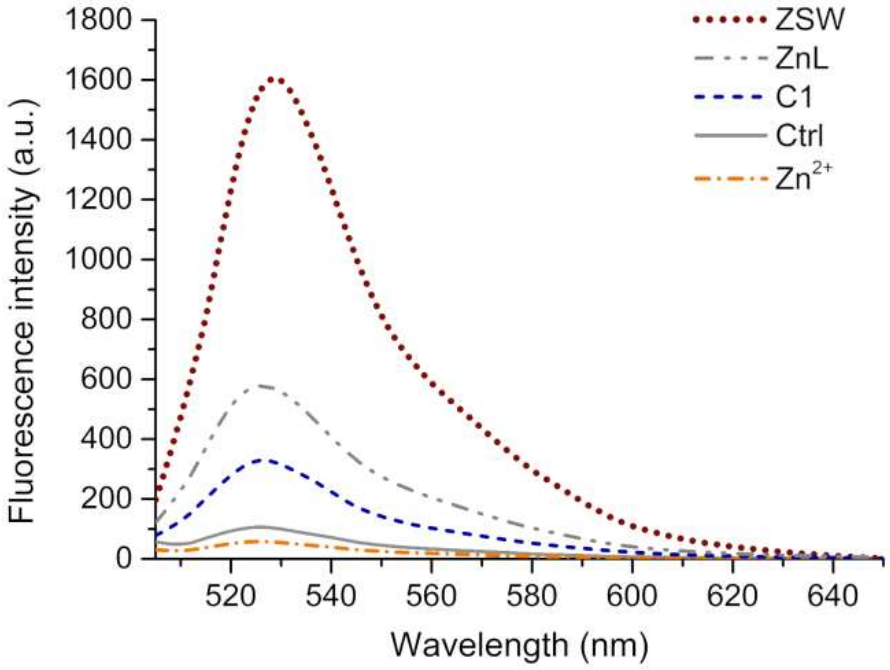

Figure 5. The intensity of the fluorescence of DCF (λ_{ex} = 485 nm, λ_{em} = 650 nm) in pH 7.4 Tris-buffer (20 mM Tris-HCl/150 mM NaCl) induced by ZSW (0.025 mM), $K_4[SiW_{12}O_{40}]$ (C1, 0.025 mM), $ZnCl_2$ (Zn^{2+}, 0.025 mM), ZnL (Zn^{2+} + Cyclen, 0.025 mM), and the control group samples.

The Gaussian 09 package was used to perform the optimization and frequency computational calculations at the DFT B3LYP/Lanl2dz level [44]. Frontier molecular orbitals represent an invaluable method for analyzing the electric characteristics of coordination compounds. The selected electron-occupied (HOMO) and -unoccupied (LUMO) MOs for $[Zn_2(4,4'\text{-bpy})(Phen)_2]^{4+}$ and the Keggin-type $[SiW_{12}O_{40}]^{4-}$ cluster are shown with energy values in Figure 6AB, respectively. For $[Zn_2(4,4'\text{-bpy})(Phen)_2]^{4+}$, the electron clouds of the HOMO were distributed on the molecular skeleton of the aromatic ring at both ends. Those of the LUMO were homogeneously well-distributed on the molecular skeleton. As for the $[SiW_{12}O_{40}]^{4-}$ cluster, the electron clouds in the HOMO were mainly accumulated in the molecular center; however, in case of the LUMO, the function groups on the outer molecular layer contributed to the electron cloud of the LUMO. As also shown in Figure 6, the values of the ΔE (E_{LUMO}–E_{HOMO}) for $[Zn_2(4,4'\text{-bpy})(Phen)_2]^{4+}$ (A) and $[SiW_{12}O_{40}]^{4-}$ cluster (B) were 0.01164 and 0.20083 a.u., respectively.

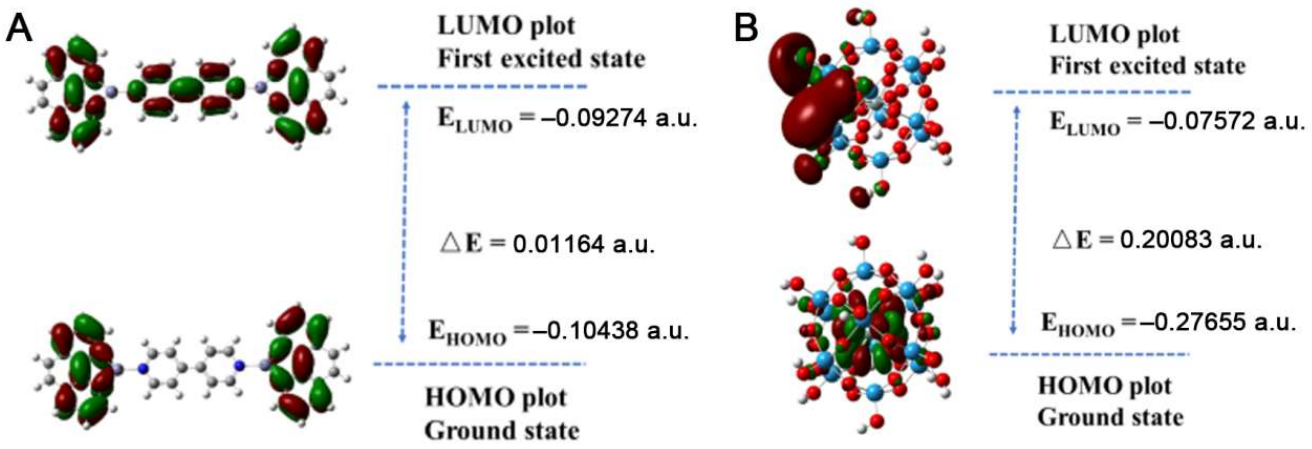

Figure 6. The selected surfaces of the molecular orbital plots (HOMO and LUMO) of $[Zn_2(4,4'\text{-bpy})(Phen)_2]^{4+}$ (**A**) and $[SiW_{12}O_{40}]^{4-}$ cluster (**B**).

In addition, the chemical potential (μ), the chemical harness (η), and the fraction number of electrons (ΔN) for the electronic transmission between A and B were also analyzed using a DFT calculation based on the literature [45,46]. Equations 2–4 were used to calculate these parameters:

$$\mu = \frac{1}{2}(E_{LUMO}+E_{HOMO}) \quad (2)$$

$$\eta = \frac{1}{2}(E_{LUMO} - E_{HOMO}) \quad (3)$$

$$\Delta N = \frac{\mu_B - \mu_A}{2(\eta_A + \eta_B)} \quad (4)$$

where μ_A and μ_B and η_A and η_B are the chemical potentials and chemical harnesses of the $[Zn_2(4,4'\text{-bpy})(Phen)_2]^{4+}$ system and $[SiW_{12}O_{40}]^{4-}$ cluster, respectively. Calculated using Equations (2)–(4), the μ and η for $[Zn_2(4,4'\text{-bpy})(Phen)_2]^{4+}$ were –0.09856 a.u. and 0.00582 a.u., respectively. As for $[SiW_{12}O_{40}]^{4-}$, the μ and η were –0.17613 a.u. and 0.10041 a.u., respectively. In addition, the ΔN between $[Zn_2(4,4'\text{-bpy})(Phen)_2]^{4+}$ and the $[SiW_{12}O_{40}]^{4-}$ cluster was –0.12242. The negative values illustrate that $[SiW_{12}O_{40}]^{4-}$ acted as an electron acceptor and $[Zn_2(4,4'\text{-bpy})(Phen)_2]^{4+}$ acted as an electron donor for the $[Zn_2(4,4'\text{-bpy})(Phen)_2]^{4+}$ and $[SiW_{12}O_{40}]^{4-}$ cluster systems. Therefore, it is likely that, as well as avoiding disturbance of the catalytic centers, the POM fragment in concert with the Zn complexes may also facilitate synergistic production of ROS.

2.3. Anti-ROS-Sensitive Tumor Activity

Since ZSW possesses excellent catalytic ability in producing ROS, ZSW may also provide good inhibition of ROS-sensitive tumor cells, such as neuroma cells [47]. Hence, the inhibitory ability of ZSW toward neuronal pheochromocytoma cells (PC12) was investigated with an MTT assay [48]. As shown in Figure 7A, the viability of PC12 cells decreased gradually with the addition of ZSW from 0 to 20 μM, which may suggest that ZSW can suppress the viability of PC12 cells. The concentration of 20 μM was chosen to carry out the following experiment. As shown in Figure 7B, the presence of ascorbic acid (VC) helped to reduce the cytotoxicity of ZSW, implying that ZSW inhibits PC12 cells through oxidation.

Next, the details of the damage from ZSW in the PC12 cells were studied by examining the cell morphological changes under the above condition. As shown in Figure 8A, the PC12 cells in the normal modality showed a polygonal shape with a network of synapses connected in all directions. However, after co-incubation with ZSW, as shown in Figure 8B, the PC12 cell morphology atrophied and spheroidized, and synapses disappeared alto-

gether with widespread death observed. As can be seen from Figure 8C, although the viable number of cells increased after the addition of VC, the morphology of the PC12 cells still changed greatly, with their bodies turning into spheres, in comparison to the normal morphology in which the synapses of those cells begin to break. Hence, it may be concluded that VC can only inhibit oxidative damage of ZSW to some extent, but cannot completely reverse the damage.

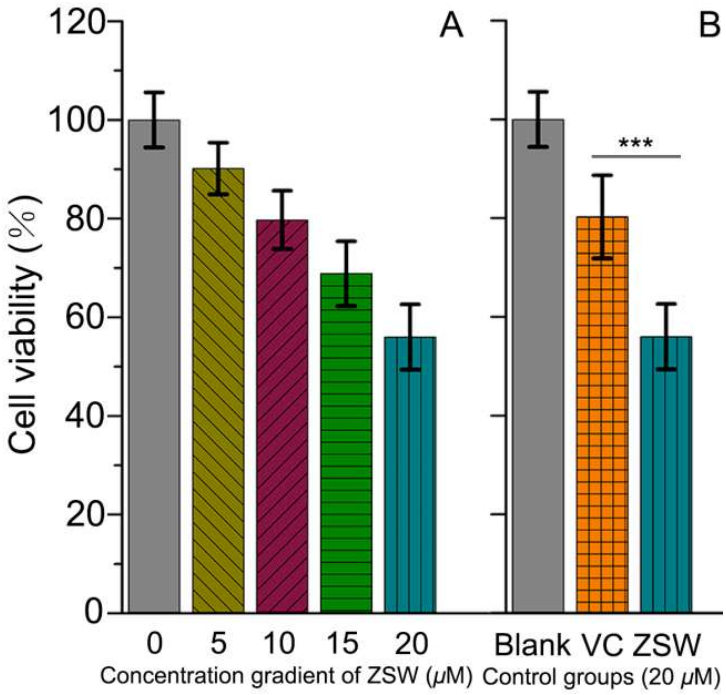

Figure 7. PC12 cell viability determined by MTT assay (**A**) after incubated by ZSW of different concentration gradients (0, 5, 10, 15, 20 μM). (**B**) Incubation by different control groups (Ctrl: blank group; VC: 20 μM ZSW + 20 μM ascorbic acid; ZSW: 20 μM ZSW). (1 μM refers to 10^{-6} mol·L^{-1}). The results are obtained from three independent experiments and presented as the mean ± standard deviation of the independent experiments. The results were compared using a two way ANOVA (*** $p \leq 0.001$).

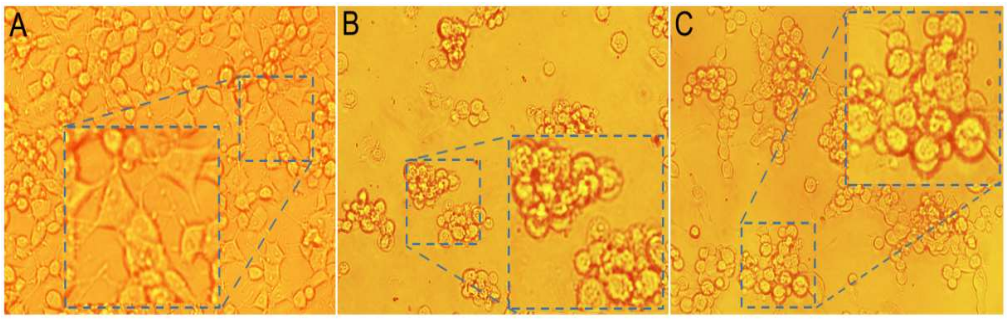

Figure 8. Photomicrographs of cells after incubated by 20 μM ZSW for (**B**), 20 μM ZSW + 20 μM ascorbic acid for (**C**) and blank group for (**A**). (inset: partial enlarged detail). (1 μM refers to 10^{-6} mol·L^{-1}).

3. Materials and Methods

3.1. Materials and Methods

All reagents employed in this work were analytically pure and used as received. 2′,7′-dichlorofluorescin diacetate (DCFH-DA), 3-(4,5-dimethyl-2-thiazolyl)- 2,5-diphenyl-2-H-tetrazolium bromide (MTT), nerve growth factor 7S (NGF-7S), and tris(hydromethyl) aminomethane (Tris) were purchased from Sigma-Aldrich Inc. (Shanghai, China). $ZnCl_2 \cdot 2H_2O$,

$Na_2WO_4{\cdot}2H_2O$, $Na_2SiO_3{\cdot}9H_2O$, 1,10-phenanthroline (Phen), 4,4′-bipyridine (4,4′-bpy), oxalic acid, and 1,4,7,10-tetraazacyclododecane (Cyclen) were obtained from J & K Scientific. Pheochromocytoma cells (PC12 cells) were purchased from the American Type Culture Collection (ATCC) (Manassas, VA, USA). Milli-Q water (Merck) was used to prepare all of the solutions, and a Millipore filter (0.22 μm) was used for all filtrations.

DCF fluorescence was conducted with a Thermo Scientific Varioskan Flash microplate reader (Thermo Fisher Scientific Inc., Singapore). The X-ray photoelectron spectrum (XPS) was tested with a PHI5000 VersaProbe instrument (Ulvac-PHI Inc., Chigasaki, Kanagawa Ken, Japan). Elemental analysis was performed on a PQEXCeII ICP-MS. IR spectra were recorded in the range of 4000–400 cm^{-1} on a Bruker Vector 22 FT-IR spectrophotometer using KBr pellets (Bruker Inc., Saarbrücken, Saarland, Germany). Intensity data of single crystals were collected on a Bruker Apex-2 diffractometer with a CCD detector using graphite-monochromatized Mo Kα radiation (λ = 0.71073 Å) at 296 K (Bruker Inc., Saarbrücken, Saarland, Germany).

3.2. Synthesis of ZSW

Two solutions were prepared separately. Solution A: $Na_2WO_4{\cdot}2H_2O$ (3.30 g, 10.00 mmol) and $Na_2SiO_3{\cdot}9H_2O$ (1.90 g, 6.70 mmol) were dissolved in water (50 mL) under stirring. Solution B: $ZnCl_2{\cdot}2H_2O$ (1.73 g, 10.00 mmol), Phen (0.52 g, 2.5 mmol), 4,4′-bpy (0.4 g, 2.0 mmol), and oxalic acid ($C_2H_2O_4{\cdot}2H_2O$, 0.25 g, 2.0 mmol) were added to water (50 mL) under stirring. The resulting mixture of B was added to solution A. The mixture was stirred for 10 min at room temperature and then the pH value was adjusted to 4.0 by adding 6 $mol{\cdot}L^{-1}$ HCl dropwise. The solution was sealed in a 25 mL Teflon-lined autoclave and kept at 150 °C for 5 days, then cooled to room temperature. Then, the colorless crystals of ZSW were separated with a 26% yield (based on $Na_2WO_4{\cdot}2H_2O$). Elemental analysis (%) calcd for $[Zn_2(4,4'\text{-bpy})(Phen)_2][SiW_{12}O_{40}]$: C 11.60, N 2.38, Si 0.80, Zn 3.62, W 62.72; found: C 11.69, N 2.44, Si 0.74, Zn 3.64, W 62.60.

3.3. X-ray Data Collection and Structure Refinement

A single ZSW crystal was mounted in an Apex-2 diffractometer (Bruker Inc., Saarbrücken, Saarland, Germany) with a CCD detector using graphite-monochromatized Mo Kα radiation (λ = 0.71073 Å) at 296 K. The SAINT software package (Bruker) was used for data integration [49]. Lorentz and polarization corrections were made in the standard way. Adsorption corrections were made using the multiscan approach with the aid of the SADABS software package (Bruker) [50]. After solving it directly, we refined the structure with the full-matrix least-squares procedure on F^2. This same refinement was performed successively along with Fourier syntheses for the remaining atoms. The SHELXL-97 package (Georg-August-Universität Göttingen, 2014, University of Göttingen, Göttingen, Niedersachsen, Germany) was used for all computations [51]. The Fourier difference map did not show the positions of any of the water molecule-related hydrogen atoms. Geometrical positioning was used for hydrogen atoms attached to C and N atoms. Isotropic refinement was done for all the hydrogen atoms using the riding model, adopting the default variables within SHELXL.

3.4. Catalytic ROS Production of ZSW

A 1 mM stock solution of DCFH-DA was prepared using a Tris-buffer (20 mM Tris–HCl/150 mM NaCl pH 7.4) and the procedure described in [52]. The same buffer was used to prepare a 4 μM HRP (horseradish peroxidase) stock solution. All samples were incubated at ambient temperature after adding 10 μM ascorbate that either contained or did not contain ZSW (0.025 mM), and then 200 μL of each solution was pipetted into one well of a black 96-well flat-bottomed microplate. DCFH-DA (100 μM) and HRP (0.04 μM) were supplemented, and then the samples were left in the dark at ambient temperature for an additional 12 h. Fluorescent spectra were captured over a range from 505 nm to 650 nm with a microplate reader (Varioskan Flash, Thermo Scientific Inc., Singapore)

with λ_{ex} = 485 nm. Spectra of $K_4[SiW_{12}O_{40}]$ (C1, 0.025 mM), $ZnCl_2$ (Zn^{2+}, 0.025 mM), $ZnCl_2$ + Cyclen (Zn^{2+} + Cyclen, 0.025 mM), and the control group were also captured for comparison under the same conditions as presented above.

3.5. Anti-ROS Sensitive Tumor Activity

PC12 cells were cultured according to a method from the literature [52]. The mature PC12 cells were incubated with ZSW at different concentration gradients from 0 to 20 μM for 24 h. Ascorbic acid and ZSW (20 μM) were incubated together as the control group. The MTT kit was then used for testing. Cell morphology was observed under an inverted fluorescence microscope.

4. Conclusions

In this study, a hybrid polyoxometalate (POM) based on a binuclear zinc complex and Keggin-type silicotungstate $[Zn_2(4,4'\text{-bpy})(Phen)_2][SiW_{12}O_{40}]$ (ZSW) (Phen = 1,10-phenanthroline; 4,4′-bpy = 4,4′-bipyridine) was synthesized successfully. The novelty of the structure is that the zinc ions in the $[Zn_2(4,4'\text{-bpy})(Phen)_2]^{2+}$ exist in tri-coordination in a solid state, and this phenomenon was first observed in POM chemistry. The synthetic method may serve as a good example for subsequent synthesis and formation of such POMs clusters. Moreover, ZSW is effective in catalyzing ROS generation, which can probably be attributed to the synergic interplay between POM fragments and zinc complexes, and further inhibits ROS-sensitive PC12 cells. The novel structure and interesting properties mean that ZSW may have broad application prospects in biochemistry and inorganic chemistry research into ROS catalysts.

Supplementary Materials: The following supporting information can be downloaded at: https://www.mdpi.com/article/10.3390/catal12070695/s1, Table S1: Selected bond lengths (Å) for ZSW, Figure S1: IR spectrum for Phen, Figure S2: IR spectrum for 4,4′-bpy.

Author Contributions: X.M. and J.H. conceived the idea of the research. X.M. and J.H. designed the molecule, X.M. and D.Z. synthesized the molecule. J.H. performed the single-crystal X-ray diffraction. X.M., X.P., X.Z. and Y.N. designed and conducted the experiments. The DFT analysis was performed by Y.W., M.W. and Y.N. analyzed the data. All authors have read and agreed to the published version of the manuscript.

Funding: This work was supported by the National Natural Science Foundation of China (Grants 22172138), the Fund for Shanxi "1331" Project, the Scientific and Technologial Innovation Programs of Higher Education Institutions in Shanxi (STIP 2020L0643 and 2020L0644), the Shanxi Province Science Foundation for Youths (Grants 201901D211453 and 20210302124333), the Research Foundation of the Chinese State Key Laboratory of Coordination Chemistry (SKLCC202204) and Taiyuan Institute of Technology Scientific Research Initial Funding.

Data Availability Statement: Crystallographic data for the structural analysis have been deposited with the Cambridge Crystallographic Data Center, CCDC reference number: 2103951 for ZSW. This data can be obtained free of charge from the Cambridge Crystallographic Data Centre via http//:www.ccdc.cam.ac.uk/data_request/cif, (accessed on 18 August 2021).

Conflicts of Interest: The authors declare no conflict of interest.

References

1. Kepp, K.P. Bioinorganic chemistry of Alzheimer's disease. *Chem. Rev.* **2012**, *112*, 5193–5239. [CrossRef] [PubMed]
2. Zhou, Z.J.; Song, J.B.; Nie, L.M.; Chen, X.Y. Reactive oxygen species generating systems meeting challenges of photodynamic cancer therapy. *Chem. Soc. Rev.* **2016**, *45*, 6597–6626. [CrossRef] [PubMed]
3. Jiang, D.W.; Ni, D.L.; Rosenkrans, Z.T.; Huang, P.; Yan, X.Y.; Cai, W.B. Nanozyme: New horizons for responsive biomedical applications. *Chem. Soc. Rev.* **2019**, *48*, 3683–3704. [CrossRef] [PubMed]
4. Wu, J.J.X.; Wang, X.Y.; Wang, Q.; Lou, Z.P.; Li, S.R.; Zhu, Y.Y.; Qin, L.; Wei, H. Nanomaterials with enzyme-like characteristics (nanozymes): Next-generation artificial enzymes (II). *Chem. Soc. Rev.* **2019**, *48*, 1004–1076. [PubMed]

5. Yao, Y.J.; Zhang, H.L.; Wang, Z.Y.; Ding, J.; Wang, S.Q.; Huang, B.Q.; Ke, S.F.; Gao, C.Y. Reactive oxygen species (ROS)-responsive biomaterials mediate tissue microenvironments and tissue regeneration. *J. Mater. Chem. B* **2019**, *7*, 5019–5037. [CrossRef] [PubMed]
6. Dickinson, L.C.; Symons, M.C.R. Electron spin resonance of haemoglobin and myoglobin. *Chem. Soc. Rev.* **1983**, *12*, 387–414. [CrossRef]
7. Xu, L.H.; Ji, X.H.; Zhao, N.; Song, C.X.; Wang, F.S.; Liu, C.H. The conjugation of Cu/Zn superoxide dismutase (SOD) to O-(2-hydroxyl) propyl-3-trimethyl ammonium chitosan chloride (O-HTCC) enhances its therapeutic potential against radiationinduced oxidative damage. *Polym. Chem.* **2016**, *7*, 1826–1835. [CrossRef]
8. Mishra, P.; Satpati, S.; Baral, S.K.; Dixit, A.; Sabat, S.C. S95C substitution in CuZn-SOD of ipomoea carnea: Impact on the structure, function and stability. *Mol. Biosyst.* **2016**, *12*, 3017–3031. [CrossRef]
9. Ma, X.; Zhang, C.; Hua, J.A.; Ma, P.T.; Wang, J.P.; Niu, J.Y. A binuclear copper-substituted phosphomolybdate with reactive oxygen species catalytic ability and antimicrobial activity. *CrystEngComm* **2019**, *21*, 394–398. [CrossRef]
10. Hua, J.A.; Yuan, X.; Ma, X.; Ma, P.T.; Wang, J.P.; Niu, J.Y. A silver-substituted phosphomolybdate prevents the growth of bacteria without affecting the balance of reactive oxygen species. *CrystEngComm* **2020**, *22*, 7832–7837. [CrossRef]
11. Ma, X.; Hua, J.A.; Xu, C.Z.; Zhang, L.M.; Wang, Y.Q.; Zhang, J.; Cao, L.H.; Niu, Y.L.; Ma, P.T. A heterogeneous catalyzed oxidase consists of zinc-substituted arsenomolybdate with reactive oxygen species catalytic ability. *J. Clust. Sci.* **2021**. [CrossRef]
12. Ma, X.; Zhou, F.T.; Yue, H.; Hua, J.A.; Ma, P.T. A nano-linear zinc-substituted phosphomolybdate with reactive oxygen species catalytic ability and antibacterial activity. *J. Mol. Struct.* **2019**, *1198*, 126865–126867. [CrossRef]
13. Du, D.Y.; Qin, J.S.; Li, S.L.; Su, Z.M.; Lan, Y.Q. Recent advances in porous polyoxometalate-based metal-organic framework materials. *Chem. Soc. Rev.* **2014**, *43*, 4615–4632. [CrossRef] [PubMed]
14. Huang, J.L.; Lin, L.Q.; Sun, D.H.; Chen, H.M.; Yang, D.P.; Li, Q.B. Bio-inspired synthesis of metal nanomaterials and applications. *Chem. Soc. Rev.* **2015**, *44*, 6330–6374. [CrossRef] [PubMed]
15. Song, Y.F.; Tsunashima, R. Recent advances on polyoxometalate-based molecular and composite materials. *Chem. Soc. Rev.* **2012**, *41*, 7384–7402. [CrossRef]
16. Yang, K.; Ying, Y.X.; Cui, L.L.; Sun, J.C.; Luo, H.; Hu, Y.Y.; Zhao, J.W. Stable aqueous Zn−Ag and Zn−polyoxometalate hybrid battery driven by successive Ag+ cation and polyoxoanion redox reactions. *Energy Storage Mater.* **2021**, *34*, 203–210. [CrossRef]
17. Gong, C.H.; Zeng, X.H.; Zhu, C.F.; Shu, J.H.; Xiao, P.X.; Xu, H.; Liu, L.C.; Zhang, J.Y.; Zeng, Q.D.; Xie, J.L. A series of organic–inorganic hybrid materials consisting of flexible organic amine modified polyoxomolybdates: Synthesis, structures and properties. *RSC Adv.* **2016**, *6*, 106248–106259. [CrossRef]
18. Jin, H.J.; Zhou, B.B.; Yu, Y.; Zhao, Z.F.; Su, Z.H. Inorganic–organic hybrids constructed from heteropolymolybdate anions and copper–organic fragments: Syntheses, structures and properties. *CrystEngComm* **2011**, *13*, 585–590. [CrossRef]
19. Weng, J.B.; Hong, M.C.; Liang, Y.C.; Shi, Q.; Cao, R. A nucleobase–inorganic hybrid polymer consisting of copper bis(phosphopentamolybdate) and cytosine. *J. Chem. Soc. Dalton Trans.* **2002**, *3*, 289–290. [CrossRef]
20. Meng, J.X.; Lu, Y.; Li, Y.G.; Fu, H.; Wang, E.B. Controllable self-assembly of four new metal–organic frameworks based on different phosphomolybdate clusters by altering the molar ratio of H_3PO_4 and Na_2MoO_4. *CrystEngComm* **2011**, *13*, 2479–2486. [CrossRef]
21. Xu, X.X.; Gao, X.; Lu, T.T.; Liu, X.X.; Wang, X.L. Hybrid material based on a coordination -complex-modified polyoxometalate nanorod (CC/POMNR) and PPy: A new visible light activated and highly efficient photocatalyst. *J. Mater. Chem. A* **2015**, *3*, 198–206. [CrossRef]
22. Feng, S.L.; Lu, Y.; Zhang, Y.X.; Su, F.; Sang, X.J.; Zhang, L.C.; You, W.S.; Zhu, Z.M. Three new strandberg-type phenylphosphomolybdate supports for immobilizing horseradish peroxidase and their catalytic oxidation performances. *Dalton Trans.* **2018**, *47*, 14060–14069. [CrossRef] [PubMed]
23. Ma, Y.; Xue, Q.; Min, S.T.; Zhang, Y.P.; Hu, H.M.; Gao, S.L.; Xue, G.L. An unusual fan-type polyanion with a silver cation located at the axial center, $[AgAs^{III}_2(As^{III}As^{V}Mo_4O_{18}(OH)_2)_3]^{11-}$. *Dalton Trans.* **2013**, *42*, 3410–3416. [CrossRef] [PubMed]
24. Li, F.Y.; Xu, L. Coordination assemblies of polyoxomolybdate cluster framework: From labile building blocks to stable functional materials. *Dalton Trans.* **2011**, *40*, 4024–4034. [CrossRef] [PubMed]
25. Chen, X.X.; Wang, Z.; Zhang, R.R.; Xu, L.Q.; Sun, D. A novel polyoxometalate-based hybrid containing a 2D $[CoMo_8O_{26}]_\infty$ structure as the anode for lithium-ion batteries. *Chem. Commun.* **2017**, *53*, 10560–10563. [CrossRef]
26. Zhao, S.; Jia, Y.Q.; Song, Y.F. Acetalization of aldehydes and ketones over $H_4[SiW_{12}O_{40}]$ and $H_4[SiW_{12}O_{40}]/SiO_2$. *Catal. Sci. Technol.* **2014**, *4*, 2618–2625. [CrossRef]
27. Sun, X.J.; Zhang, J.; Yuan, X.Z.; Fu, Z.Y. A silicotungstatebased copper–viologen hybrid photocatalytic compound for efficient degradation of organic dyes under visible light. *CrystEngComm* **2019**, *21*, 5563–5567. [CrossRef]
28. Ma, X.; Zhou, Y.J.; Yuan, X.R.; Miao, Y.J.; Zhao, Q.; Hua, J.A.; Ma, P.T. An organic-inorganic hybrid nanoscale phosphotungstate with reactive oxygen species catalytic ability. *Inorg. Nano-Met. Chem.* **2021**, *51*, 332–339. [CrossRef]
29. Hua, J.A.; Wei, X.M.; Bian, Y.J.; Ma, X.; Hao, L.; Sun, J.R.; Fan, J.J.; Niu, Y.L.; Wang, Y.Q. A nanoscale polymolybdate built by two hexavacant Keggin-type fragments via a novel $\{Ca_6P_6O_{38}\}$ cluster with β-sheet conformation modulation ability. *CrystEngComm* **2022**, *24*, 3153–3159. [CrossRef]
30. Faller, P.; Hureau, C.; La Penna, G. Metal ions and intrinsically disordered proteins and peptides: From Cu/Zn amyloid-β to general principles. *Acc. Chem. Res.* **2014**, *47*, 2252–2259. [CrossRef]

31. Ma, X.; Zhao, Q.; Wang, B.; Li, D.N.; Zhou, Y.J.; Hua, J.A.; Ma, P.T. A hybrid silicotungstate based on tri-coordination copper complex and Keggin type cluster with reactive oxygen species catalytic ability. *J. Mol. Struct.* **2020**, *1206*, 127714–127716. [CrossRef]
32. Szilágyi, I.M.; Hange, F.; Madarász, J.; Pokol, G. In situ HT-XRD study on the formation of hexagonal ammonium tungsten bronze by partial reduction of ammonium paratungstate tetrahydrate. *Eur. J. Inorg. Chem.* **2006**, *17*, 3413–3418. [CrossRef]
33. Zheng, S.T.; Zhang, J.; Juan, J.M.; Yuan, D.Q.; Yang, G.Y. Poly(polyoxotungstate)s with 20 nickel centers: From nanoclusters to one-dimensional chains. *Angew. Chem. Int. Ed. Engl.* **2009**, *48*, 7176–7179. [CrossRef] [PubMed]
34. Brown, I.D.; Altermatt, D. Bond-valence parameters obtained from a systematic analysis of the inorganic crystal structure database. *Acta Crystallogr. B Struct. Sci.* **1985**, *41*, 244–247. [CrossRef]
35. Shields, G.P.; Raithby, P.R.; Allen, F.H.; Motherwell, W.D.S. The assignment and validation of metal oxidation states in the Cambridge structural database. *Acta Crystallogr. B Struct. Sci.* **2000**, *56*, 455–465. [CrossRef]
36. Ma, X.; Hua, J.A.; Wang, K.; Zhang, H.M.; Zhang, C.L.; He, Y.F.; Guo, Z.J.; Wang, X.Y. Modulating conformation of Aβ peptide: An effective way to prevent protein-misfolding disease. *Inorg. Chem.* **2018**, *57*, 13533–13543. [CrossRef]
37. Streb, C.; Ritchie, C.; Long, D.L.; Kögerler, P.; Cronin, L. Modular assembly of a functional polyoxometalate-based open framework constructed from unsupported AgI–AgI interactions. *Angew. Chem. Int. Ed. Engl.* **2007**, *46*, 7579–7582. [CrossRef]
38. Ma, X.; Bian, Y.J.; Zhou, Y.J.; Zhao, Q.; Tian, Y.; Hua, J.A.; Ma, P.T. Synthesis, characterization, and catalytic property of a hybrid nanoscale polyoxoniobate. *J. Clust. Sci.* **2021**, *32*, 613–620. [CrossRef]
39. MacDonald, L.; Rausch, B.; Symes, M.D.; Cronin, L. Selective hydrogenation of nitroarenes using an electrogenerated polyoxometalate redox mediator. *Chem. Commun.* **2018**, *54*, 1093–1096. [CrossRef]
40. Zheng, S.T.; Yuan, D.Q.; Zhang, J.; Yang, G.Y. Combination of lacunary polyoxometalates and high-nuclear transition metal clusters under hydrothermal conditions. 3. Structure and characterization of $[Cu(enMe)_2]_2\{[Cu(enMe)_2(H_2O)]_2[Cu_6(enMe)_2(B\text{-}\alpha\text{-}SiW_9O_{34})_2]\}\cdot 4H_2O$. *Inorg. Chem.* **2007**, *46*, 4569–4574. [CrossRef]
41. Wang, L.M.; Wang, Y.; Fan, Y.; Xiao, L.N.; Hu, Y.Y.; Gao, Z.M.; Zheng, D.F.; Cui, X.B.; Xu, J.Q. The design, syntheses and characterization of a series of hybrids based on polyoxometalates and metal complexes. *CrystEngComm* **2014**, *16*, 430–440. [CrossRef]
42. Wang, X.H.; Wang, X.Y.; Zhang, C.L.; Jiao, Y.; Guo, Z.J. Inhibitory action of macrocyclic platiniferous chelators on metalinduced Aβ aggregation. *Chem. Sci.* **2012**, *3*, 1304–1312. [CrossRef]
43. Zhao, J.S.; Wang, Y.; Zhou, J.W.; Qi, P.F.; Li, S.W.; Zhang, K.X.; Feng, X.; Wang, B.; Hu, C.W. A copper(ii)-based MOF film for highly efficient visible-light-driven hydrogen production. *J. Mater. Chem. A* **2016**, *4*, 7174–7177. [CrossRef]
44. Frisch, M.J.; Trucks, G.W.; Schlegel, H.B.; Scuseria, G.E.; Robb, M.A.; Cheeseman, J.R.; Scalmani, G.; Barone, V.; Mennucci, B.; Petersson, G.A.; et al. Gaussian 09 Revision D. Available online: https://gaussian.com/ (accessed on 29 April 2022).
45. Padmanabhan, J.; Parthasarathi, R.; Subramanian, V.; Chattaraj, P.K. Group philicity and electrophilicity as possible descriptors for modeling ecotoxicity applied to chlorophenols. *Chem. Res. Toxicol.* **2006**, *19*, 356–364. [CrossRef]
46. Wang, Y.Q.; Han, Q.Q.; Zhang, H.M.; Yan, Y.Y. Evaluation of the binding interactions of p-acetylaminophenol, aspirin, ibuprofen and aminopyrine with norfloxacin from the view of antipyretic and anti-inflammatory. *J. Mol. Liq.* **2020**, *312*, 113397. [CrossRef]
47. Hua, J.A.; Wei, X.M.; Ma, X.; Jiao, J.Z.; Chai, B.H.; Wu, C.B.; Zhang, C.L.; Niu, Y.L. A $\{Cd_4Cl_2O_{14}\}$ cluster functionalized sandwich-type tungstoarsenate as a conformation modulator for misfolding Aβ peptides. *CrystEngComm* **2022**, *24*, 1171–1176. [CrossRef]
48. Liu, J.C.; Wang, J.F.; Han, Q.; Shangguan, P.; Liu, L.L.; Chen, L.J.; Zhao, J.W.; Streb, C.; Song, Y.F. Multicomponent self-assembly of a giant heterometallic polyoxotungstate supercluster with antitumor activity. *Angew. Chem. Int. Ed.* **2021**, *60*, 11153–11157. [CrossRef]
49. Bruker S.M.A.R.T. *SAINT (Version 6.02)*; Bruker AXS Inc.: Madison, WI, USA, 2000.
50. Brese, N.E.; O'Keeffe, M. Bond-valence parameters for solids. *Acta Crystallogr. B Struct. Sci.* **1991**, *47*, 192–197. [CrossRef]
51. Sheldrick, G.M. *SHEXTL-97, Programs for Crystal Structure Refinements*; University of Göttingen: Göttingen, Germany, 1997.
52. Ma, X.; Wang, Y.Q.; Hua, J.A.; Xu, C.Y.; Yang, T.; Yuan, J.; Chen, G.Q.; Guo, Z.J.; Wang, X.Y. A β-sheet-targeted theranostic agent for diagnosing and preventing aggregation of pathogenic peptides in Alzheimer's disease. *Sci. China Chem.* **2020**, *63*, 73–82. [CrossRef]